

# Type-III Dirac fermions in $\text{Hf}_x\text{Zr}_{1-x}\text{Te}_2$ topological semimetal candidate

Cite as: J. Appl. Phys. 129, 075104 (2021); <https://doi.org/10.1063/5.0038799>

Submitted: 26 November 2020 . Accepted: 04 February 2021 . Published Online: 19 February 2021

 Sotirios Fragkos,  Polychronis Tsipas,  Evangelia Xenogiannopoulou,  Yerassimos Panayiotatos, and  Athanasios Dimoulas



View Online



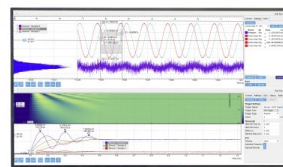
Export Citation



CrossMark

Challenge us.

What are your needs for  
periodic signal detection?



Zurich  
Instruments



# Type-III Dirac fermions in $\text{Hf}_x\text{Zr}_{1-x}\text{Te}_2$ topological semimetal candidate

Cite as: J. Appl. Phys. 129, 075104 (2021); doi: 10.1063/5.0038799

Submitted: 26 November 2020 · Accepted: 4 February 2021 ·

Published Online: 19 February 2021



View Online



Export Citation



CrossMark

Sotirios Fragkos,<sup>1,2,a)</sup> Polychronis Tspas,<sup>1</sup> Evangelia Xenogiannopoulou,<sup>1</sup> Yerassimos Panayiotatos,<sup>2</sup> and Athanasios Dimoulas<sup>1,3,a)</sup>

## AFFILIATIONS

<sup>1</sup>Institute of Nanoscience and Nanotechnology, National Center for Scientific Research ‘Demokritos’, 15310 Athens, Greece

<sup>2</sup>Department of Mechanical Engineering, University of West Attica, 12241 Athens, Greece

<sup>3</sup>Department of Physics, National and Kapodistrian University of Athens, 15772 Athens, Greece

**Note:** This paper is part of the Special Topic on Topological Materials and Devices.

**a) Authors to whom correspondence should be addressed:** s.fragkos@inn.demokritos.gr; s.fragkos@uniwa.gr; and a.dimoulas@inn.demokritos.gr

## ABSTRACT

Topological semimetals host interesting new types of low-energy quasiparticles such as type-I and type-II Dirac and Weyl fermions. Type-III topological semimetals can emerge exactly at the border between type-I and II, characterized by a line-like Fermi surface and a flat energy dispersion near the topological band crossing. Here, we theoretically predict that 1T-HfTe<sub>2</sub> and 1T-ZrTe<sub>2</sub> transition metal dichalcogenides are type-I and type-II DSMs, respectively. By alloying the two materials, a new Hf<sub>x</sub>Zr<sub>1-x</sub>Te<sub>2</sub> alloy with type-III Dirac cone emerges at  $x = 0.2$ , in combination with 1% in-plane compressive strain. By imaging the electronic energy bands with *in situ* angle-resolved photo-emission spectroscopy of this random alloy with the desired composition, grown by molecular beam epitaxy on InAs(111) substrates, we provide experimental evidence that the top of type-III Dirac cone lies at—or very close to—the Fermi level.

Published under license by AIP Publishing. <https://doi.org/10.1063/5.0038799>

## I. INTRODUCTION

Topological 3D Dirac semimetals (DSMs) and Weyl semimetals (WSM), often called “3D graphenes,” exhibit Dirac-like cones with linear dispersion in all three dimensions in  $k$ -space.<sup>1</sup> DSMs are classified either as type-I DSM<sup>1</sup> with untilted or slightly tilted Dirac cone and a point-like Fermi surface or as type-II DSM.<sup>1</sup> In the latter case, the Dirac cone is overtilted producing a finite Fermi surface consisting of electron and hole pockets which cross at the Dirac point (DP) (Fig. 1). Yet, a type-III DSM<sup>2-4</sup> merges as a theoretical possibility exactly at the borders between type-I and type-II, characterized by a unique line-like Fermi surface and a flat energy dispersion along one direction in the Brillouin zone (BZ) (Fig. 1).

The Fermi surface topology depends sensitively on the position of the Fermi level relative to the energy degeneracy points (Dirac points) of the DSM/WSM. Near the Dirac point, the system can undergo an electronic (Lifshitz) phase transition<sup>5,6</sup> under the influence of external stimuli (e.g., temperature, pressure, etc.). At the critical conditions for the transition, the Fermi surface topology

can drastically change<sup>7-10</sup> with important consequences in electronic and thermoelectric transport. Most commonly observed is a temperature driven Lifshitz transition from a hole-like to electron-like Fermi surface,<sup>7</sup> e.g., in ZrTe<sub>5</sub><sup>7,8</sup> and HfTe<sub>5</sub><sup>9</sup> accompanied with resistivity and thermopower anomalies at the critical temperature. An anomalous Nernst effect has also been observed<sup>10</sup> in TaP and TaAs WSMs, which has been correlated to a Lifshitz transition. A quite different Lifshitz transition is expected in a type-III DSM. The system can easily make the transition from a type-I to type-II DSM associated with a big change in the Fermi surface from a point-like to a needle-like configuration, likely accompanied by resistivity and thermopower changes as in the case of ZrTe<sub>5</sub>.<sup>8</sup> The latter changes could be accessible to (thermo)electric transport experiments; therefore, there is a strong motivation to search for type-III DSMs (and WSMs). This search is also motivated by the spectacular predictions,<sup>2,3</sup> that type-III DSMs (i.e., black phosphorus,<sup>11</sup> Zn<sub>2</sub>In<sub>2</sub>S<sub>5</sub>)<sup>12</sup> could be the solid state (or fermionic) analog of the black hole event horizon potentially generating “Hawking

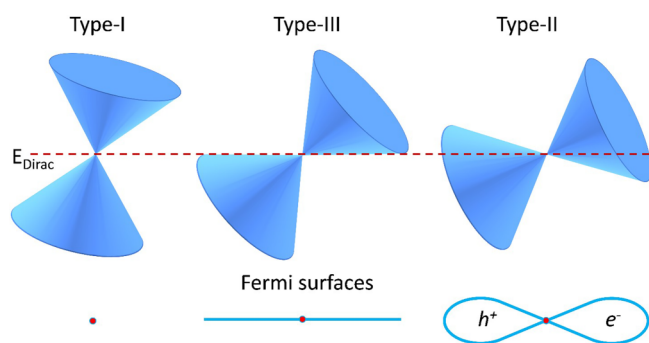


**FIG. 1.** Schematic illustration of the different types of DSMs. Type-III is at the border between type-I and type-II, characterized by a line-like Fermi surface and flat energy dispersion at the Fermi level.

radiation” at relatively high “Hawking temperature,”<sup>2</sup> showing promise for new exotic physics and applications. Although a type-III Dirac crossing was only a theoretical possibility up to now, experimental evidence has been recently obtained in strained epitaxial SnTe,<sup>13</sup> between its two uppermost valence bands, 1.83 eV below the Fermi level using synchrotron ARPES and also in artificial photonic orbital graphene lattices.<sup>14</sup>

Prototypical topological Dirac semimetals are 3D crystal structures and are typically grown as bulk crystals,<sup>15,16</sup> usually suffering from heteroepitaxial defects which yield discontinuous films with poor crystalline quality. Discovering and engineering topological semimetals from the family of two-dimensional transition metal dichalcogenides (TMDs) could open the way for exploitation of their topological properties by fabricating thin epitaxial films and devices on suitable substrates via van der Waals epitaxy. Previous report from our team<sup>17,18</sup> provide the first experimental evidence by angle-resolved photoemission spectroscopy (ARPES) that few-layer 1T-HfTe<sub>2</sub><sup>17</sup> and 1T-ZrTe<sub>2</sub><sup>18</sup> epitaxially grown by molecular beam epitaxy (MBE) are 3D DSMs. More specifically, we observed that linearly dispersing bands along  $\Gamma$ K and  $\Gamma$ M directions in the plane of the film cross at the Fermi level indicating the existence of Dirac fermions even down to the ultimate 2D limit of 1 ML with the DP located at—or very close to—Fermi level, which is notably different than theory which predicts the DP well above it.

The question about the possibility of topological properties in HfTe<sub>2</sub> and ZrTe<sub>2</sub> remains open. Synchrotron ARPES studies on single crystals of K and Cr doped HfTe<sub>2</sub><sup>19,20</sup> and ZrTe<sub>2</sub>,<sup>21</sup> respectively, show no clear signs of Dirac-like features compared to the epitaxially grown films,<sup>17,18</sup> while others, by combining synchrotron ARPES<sup>22</sup> on 1T-ZrTe<sub>2</sub> single crystals with DFT calculations suggest that ZrTe<sub>2</sub> is a DSM. From the aforementioned discussion, it is concluded that doping by intercalation changes drastically both crystal and electronic structure of these materials, so an associated change of the topological properties of HfTe<sub>2</sub> and ZrTe<sub>2</sub> cannot be excluded. Despite the controversy, evidence is accumulating in favor of non-trivial topology in these materials. Magnetotransport measurements indicate that both HfTe<sub>2</sub><sup>23</sup> and ZrTe<sub>2</sub><sup>24,25</sup> are topological materials. A recent theoretical study<sup>26</sup>

using a newly developed formalism known as topological quantum chemistry<sup>27</sup> predicts that both HfTe<sub>2</sub> and ZrTe<sub>2</sub> are topological semimetals. Note, however, that others<sup>28,29</sup> identified HfTe<sub>2</sub> as DSM but ZrTe<sub>2</sub> as topological crystalline insulator. The range of applications of topological materials including ZrTe<sub>2</sub> and HfTe<sub>2</sub> is widely open. Several of these materials have large spin Berry curvature as a combined result of their electronic band structure and large spin-orbit coupling. Consequently, they have large spin hall conductivity<sup>30,31</sup> which makes them suitable candidates for charge to spin conversion in combined topological/ferromagnet spin orbit torque (SOT) devices. This could lead to all electrically driven SOT spintronic devices for storage and processing of information. Replacing heavy metals like Pt or Ta typically used in SOT devices by two-dimensional TMDs, it is expected that the energy efficiency for charge to spin conversion will be improved.<sup>31</sup> This has already been demonstrated for the WTe<sub>2</sub>/permalloy system.<sup>32</sup> Other ditellurides like HfTe<sub>2</sub> and ZrTe<sub>2</sub> may follow a similar trend manifesting their suitability for spintronics applications. In a similar perspective, a recent work<sup>24</sup> reports anomalous hall effect of ZrTe<sub>2</sub> in proximity with a magnetic material, which could be considered as a sign that a quantum anomalous Hall effect (QAHE) is possible in this system as already predicted for topological/ferromagnetic materials combinations. This opens the possibility to utilize the dissipationless chiral edge states of a QAHE system to create energy efficient spintronic devices without the need of a magnetic field. In a different perspective,<sup>33</sup> it has been predicted that monolayer 1T-HfTe<sub>2</sub> nanosheets are highly selective toward the sensing of environmental hazardous NO gas which also plays an active role in several physiological processes, and thus, could have important applications in the area of environment and medicine.

In this paper, our first-principles calculations reveal that HfTe<sub>2</sub> and ZrTe<sub>2</sub> are type-I and type-II DSMs, respectively, which creates the prospect that by alloying the two materials, a new Hf<sub>x</sub>Zr<sub>1-x</sub>Te<sub>2</sub> type-III DSM material will emerge. After a systematic investigation of Hf<sub>x</sub>Zr<sub>1-x</sub>Te<sub>2</sub> energy bands as a function of composition and strain, a type-III Dirac cone with a line-like Fermi surface is predicted to form at 20% concentration of Hf in combination with 1% in-plane compressive strain. Furthermore, by imaging the electronic energy bands with *in situ* ARPES of this layered compound at the desired composition  $x=0.2$ , grown by MBE on the InAs(111) substrate, we provide experimental evidence that the top of type-III Dirac cone lies at—or very close to—the Fermi level.

## II. FIRST-PRINCIPLES CALCULATIONS

HfTe<sub>2</sub> and ZrTe<sub>2</sub> belong to the 2D layered 1T octahedral family with space group  $P\bar{3}m1$  (No. 164). In order to reveal the topological nature of the Dirac cones in these materials, we present *ab initio* calculations of electronic structure and perform symmetry analysis. The first-principles calculations were performed using the Vienna *Ab initio* Simulation Package<sup>34,35</sup> (VASP). The generalized-gradient approximation with Perdew–Burke–Ernzerhof<sup>36</sup> (PBE) parameterization was used as exchange-correlation functional. Our study of the electronic band structure is based on the experimental lattice constants of Refs. 17 and 18, measured by synchrotron x-ray diffraction, instead of the equilibrium ones from DFT calculations.

The kinetic energy cutoff was set at 500 eV, and the reciprocal space was sampled using the Monkhorst–Pack scheme<sup>37</sup> employing a  $11 \times 11 \times 11$   $k$ -point mesh. Spin-orbit coupling (SOC) was included for the band structure calculations. We used Hf  $d$  orbitals, Zr  $d$  orbitals, and Te  $p$  orbitals to construct Wannier functions using the Wannier90 code,<sup>38,39</sup> and the band structures and Fermi surfaces were obtained by the WannierTools software.<sup>40</sup>

### A. Electronic band structure of HfTe<sub>2</sub> and ZrTe<sub>2</sub>

VASP2Trace code<sup>26</sup> was used to examine the topology and calculate the irreducible representations at the high-symmetry points of VASP wavefunctions. The decomposition of these irreducible representations for both HfTe<sub>2</sub> and ZrTe<sub>2</sub>, moving along the  $\Gamma$ -A direction, were deduced from the BANDREP program<sup>27,41,42</sup> of the Bilbao Crystallographic Server. From these calculations [Figs. 2(a) and 2(b)], it is inferred that gapless crossing occurs because the two bands belong to different irreducible representations ( $\bar{\Delta}_6$  and  $\bar{\Delta}_4\bar{\Delta}_5$ ) which prohibits hybridization and gap opening. As a

result, a pair of fourfold degenerate Dirac nodes is generated which is protected by  $C_3$  rotational symmetry along the  $c$  axis<sup>43</sup> at  $(0,0, \pm 0.036c^*)$  and  $(0,0, \pm 0.228c^*)$  for HfTe<sub>2</sub> and ZrTe<sub>2</sub>, respectively. The crossings are created via band inversion<sup>43</sup> at positions which are symmetrically placed with respect to  $\Gamma$  along the  $\Gamma$ -A ( $k_z$ ) direction of the BZ, thus defining a pair of DPs. In Figs. 2(c) and 2(d), the electronic band structures around the DPs are visualized in the  $k_z$ - $k_x$  plane.

Further calculations of the 2D and 3D Fermi surfaces are presented in Fig. 3. By setting the chemical potential at the position of the Dirac points, a point-like Fermi surface [the inset of Figs. 3(a) and 3(c)] is revealed in the case of HfTe<sub>2</sub> characteristic to a type-I Dirac semimetal. On the other hand, needle-like electron and hole pockets are formed in the case of ZrTe<sub>2</sub> [Figs. 3(b) and 3(d)], which touch at the DP, indicating that ZrTe<sub>2</sub> is type-II DSM.

It should be mentioned that, unlike Weyl semimetals, Dirac semimetals do not possess Berry phase or Berry curvature since the three-dimensional Dirac nodes are not chiral since they are the sum of two Weyl nodes of opposite chirality at the same energy

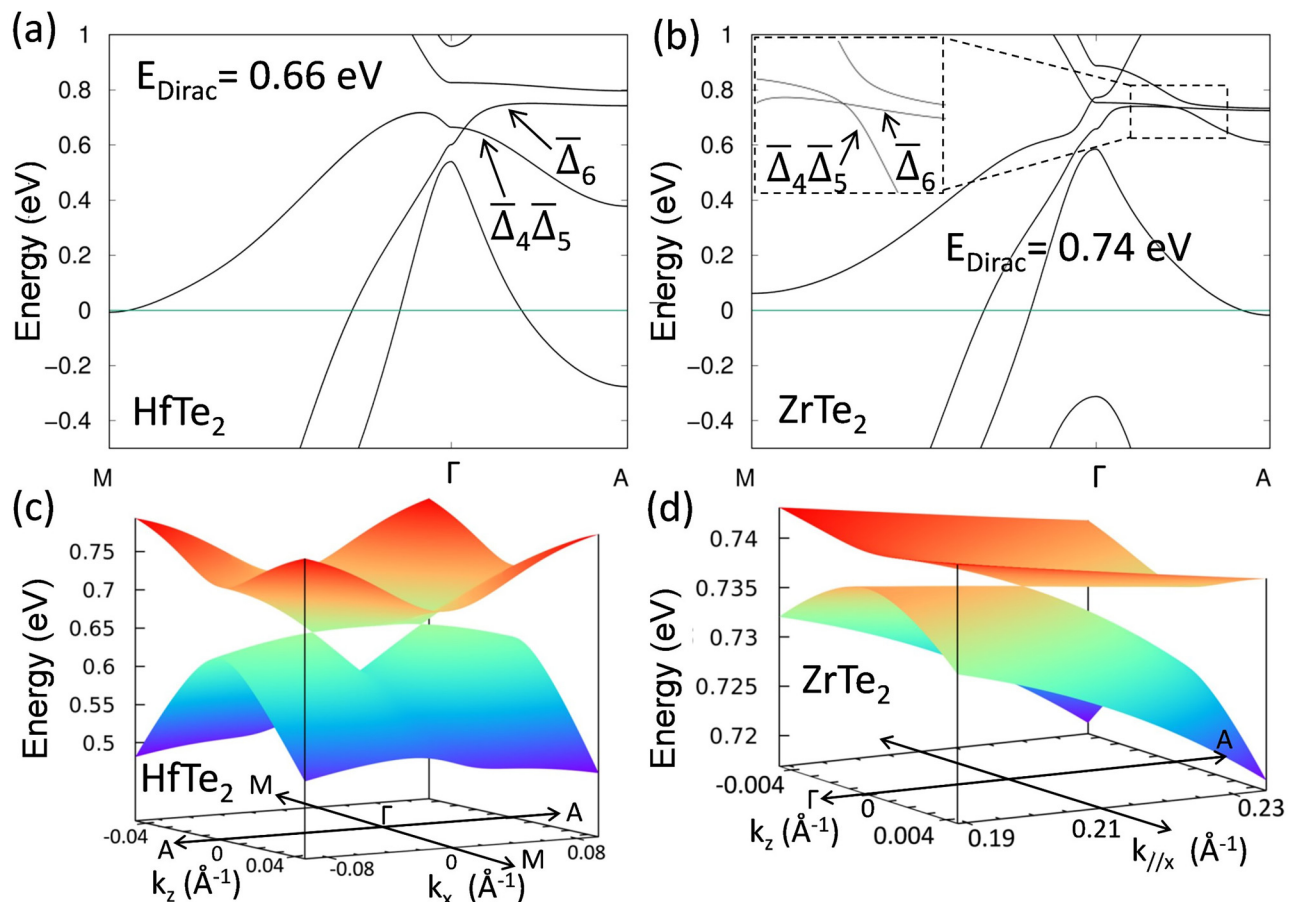


**FIG. 2.** Band structure of (a) HfTe<sub>2</sub> and (b) ZrTe<sub>2</sub> along the M- $\Gamma$ -A direction of the BZ, where valence and conduction bands which belong to different irreducible representations cross each other. (c) and (d) show the energy dispersion in the  $k_z$ - $k_x$  plane near the crossings for HfTe<sub>2</sub> and ZrTe<sub>2</sub>, respectively.

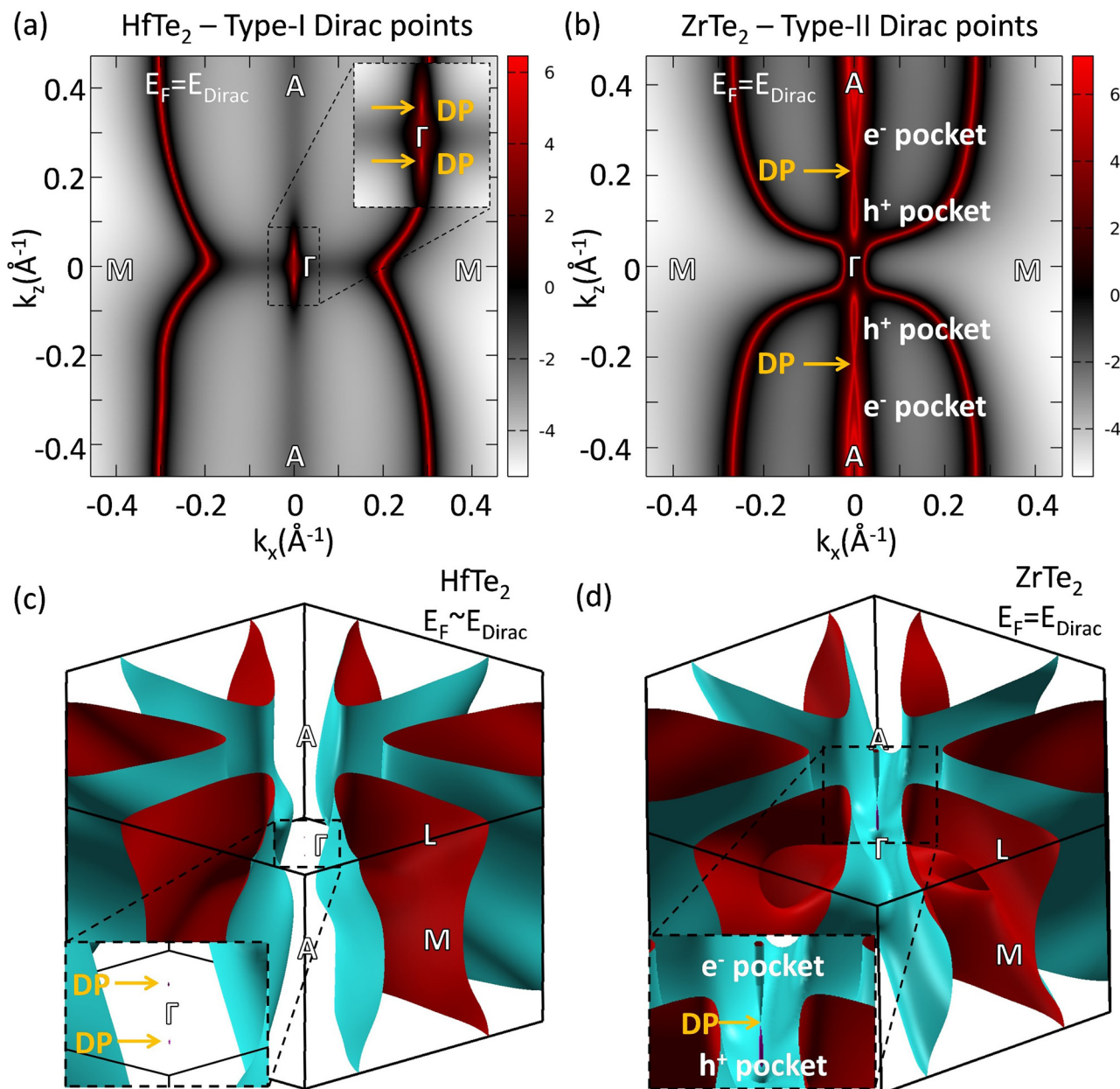


**FIG. 3.** The 2D [(a) and (b)] and 3D [(c) and (d)] Fermi surface of HfTe<sub>2</sub> and ZrTe<sub>2</sub> when the chemical potential is set to nearly coincide with the DP energy. The point-like features in the inset of (c) indicate a type-I DSM for HfTe<sub>2</sub>. The needle-like  $e^-$  and  $h^+$  pockets in ZrTe<sub>2</sub> [the inset of (d)] define the DP at the touching point indicating type-II DSM.

and momentum. Thus, the topological charge is zero everywhere in momentum space within the Brillouin zone. In addition, unlike Weyl semimetals, Dirac semimetals are protected only by underlying crystallographic symmetry, otherwise they become gapped. In our case, this role is played by the  $C_3$  rotational symmetry.

### B. The Hf<sub>0.2</sub>Zr<sub>0.8</sub>Te<sub>2</sub> type-III Dirac semimetal state

By alloying the two materials (HfTe<sub>2</sub> and ZrTe<sub>2</sub>), a new Hf<sub>x</sub>Zr<sub>1-x</sub>Te<sub>2</sub> material with type-III Dirac cone with a line-like Fermi surface could emerge at a certain composition. The electronic band structure of the Hf<sub>x</sub>Zr<sub>1-x</sub>Te<sub>2</sub> alloy was calculated by a

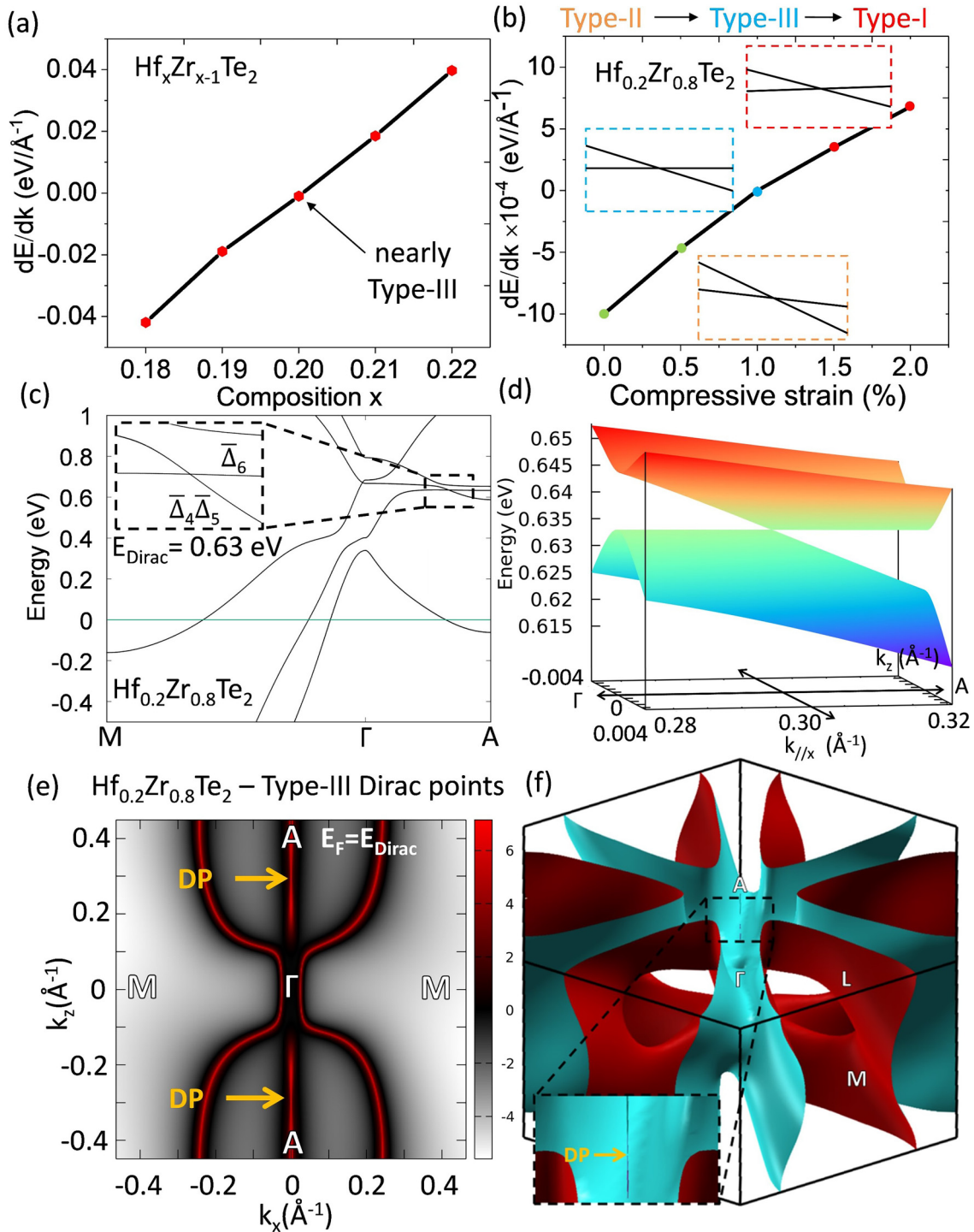


**FIG. 4.** (a) Systematic investigation of  $\text{Hf}_x\text{Zr}_{1-x}\text{Te}_2$  energy bands as a function of composition and (b) of compressive strain, where the orange, blue, and red insets show the evolution of the Dirac cone (type-II, type-III, and type-I, respectively). (c) Electronic band structure of  $\text{Hf}_{0.2}\text{Zr}_{0.8}\text{Te}_2$  with 1% in-plane compressive strain along the M- $\Gamma$ -A direction. The inset indicates the type-III band crossing between valence and conduction bands featuring a line-like Fermi surface. (d) The 3D band structure near the crossing point. (e) and (f) The 2D and 3D Fermi surfaces of  $\text{Hf}_{0.2}\text{Zr}_{0.8}\text{Te}_2$ , respectively.

linear interpolation of tight-binding model matrix elements<sup>44–46</sup> of  $\text{HfTe}_2$  and  $\text{ZrTe}_2$  generated by the Wannier90 code,<sup>38,39</sup> that is, in order to construct the tight-binding model of  $\text{Hf}_x\text{Zr}_{1-x}\text{Te}_2$  random alloy for each matrix element  $t_{ij,\text{Hf}_x\text{Zr}_{1-x}\text{Te}_2}$  we used a linear interpolation of the form  $t_{ij,\text{Hf}_x\text{Zr}_{1-x}\text{Te}_2} = x \cdot t_{ij,\text{HfTe}_2} + (1-x) \cdot t_{ij,\text{ZrTe}_2}$ , where  $x$  is the Hf concentration and since the two materials have very similar crystal structures, the experimental lattice constants of Ref. 18 were used. The proposed approach could be sensitive to a possible asymmetry between the Zr and Hf radii. Note, however, that the van der Waals radii<sup>47</sup> of Hf and Zr are 2.53 and 2.52 Å, respectively, so their difference is negligible. In addition, if we consider the Wigner–Seitz radii provided by the PBE pseudopotentials,<sup>36</sup> then Hf and Zr have the same value of 1.614 Å. This is also true for the empirical atomic radii with a value of 1.55 Å.<sup>48</sup> Therefore, the radii of Hf and Zr are very similar and we expect no big asymmetry in size that will adversely affect our calculations. Tight-binding elements contain all important information<sup>44–46</sup> for an interpolation to cover all changes of the electronic structure between the two end point materials. Furthermore, Wannier functions are critical for the study and classification of topological materials,<sup>26,27,49–52</sup> thus making this approach suitable and reliable for calculating their alloys. Previously, the same method was used to investigate the electronic band structure of  $\text{BiTlSe}_{1-x}\text{S}_x$  topological insulator<sup>44</sup> and of the transition metal dichalcogenide  $\text{Mo}_x\text{W}_{1-x}\text{Te}_2$  topological WSM<sup>46</sup> and was in excellent agreement with their ARPES measurements.

A systematic investigation of  $\text{Hf}_x\text{Zr}_{1-x}\text{Te}_2$  energy bands as a function of the composition was made [Fig. 4(a)]. Hf doping is not efficient enough to completely flatten the valence band around the crossing point. The optimum value of  $x=0.2$  produces a slope  $dE/dk = -0.001 \text{ eV/\AA}^{-1}$ , a value quite close to the ideal of a type-III crossing. Therefore, we applied an in-plane compressive strain [Fig. 4(b)] resulting in an out-of-plane expansion of the film and the van der Waals gap, which in turn weakens the interlayer interaction and flattens the bands along the  $\Gamma$ -A direction. More precisely, by applying 1% in-plane compressive strain, the  $\bar{\Delta}_6$  valence band is flat (dispersionless) near the DP while the conduction  $\bar{\Delta}_4\bar{\Delta}_5$  band disperses downward crossing the flatband [Figs. 4(d) and 5(c)]. Plotting the 2D [Fig. 4(e)] and 3D [Fig. 4(f)] Fermi surfaces, line-like electron and hole pockets are visible and cross at  $(0,0, \pm 0.332c^*)$ , which satisfies the condition for the formation of type-III Dirac cones. Therefore, the in-plane strain could be considered as a switching mechanism for shifting from type-I to type-II DSM as indicated in Fig. 4(b). It should be reminded that such a change is highly desirable since it constitutes an electronic Lifshitz phase transition with important consequences in electronic and thermoelectric transport (see Sec. I).

The crystal structures of 1T  $\text{HfTe}_2$ ,  $\text{ZrTe}_2$ , and  $\text{Hf}_{0.2}\text{Zr}_{0.8}\text{Te}_2$  are illustrated in Fig. 5, where the Hf atomic positions in  $\text{Hf}_{0.2}\text{Zr}_{0.8}\text{Te}_2$  are randomly selected.

### III. GROWTH AND ELECTRONIC BAND IMAGING OF $\text{Hf}_{0.2}\text{Zr}_{0.8}\text{Te}_2$ ALLOY

In this section, we provide experimental evidence that few-layer  $\text{Hf}_x\text{Zr}_{1-x}\text{Te}_2$  compound can be grown with the desired composition  $x=0.2$  using MBE on  $\text{InAs}(111)$  substrates. The  $\text{InAs}$

(111)/ $\text{Si}(111)$  substrates were chemically cleaned in a 5 N HF solution in isopropyl alcohol for 5 min to etch the surface oxide and subsequently rinsed in isopropyl alcohol for 30 s in order to avoid reoxidation of the substrate. An annealing step at 400 °C in ultra-high vacuum (UHV) follows to get a clean and flat  $\text{InAs}(111)$  surface observed by reflection high-energy electron-diffraction (RHEED). Where appropriate, mild  $\text{Ar}^+$  sputtering was used ( $E \approx 1.5 \text{ keV}$ ,  $p \approx 2 \times 10^{-5} \text{ mbar}$ ,  $t \approx 30 \text{ s}$ ) prior the annealing step to obtain a clean surface as evidenced by a  $2 \times 2$  reconstruction in RHEED pattern attributed to In surface vacancies.<sup>53</sup> It should be noted that starting with a clean  $2 \times 2$   $\text{InAs}(111)$  reconstructed surface is an important requirement in order to obtain a good registry of the epitaxial film with the substrate with an in-plane orientation. The same procedure was previously applied in  $\text{ZrTe}_2$ ,<sup>18</sup>  $\text{MoTe}_2$ ,<sup>54</sup> and  $\text{TiTe}_2$ <sup>55</sup> two-dimensional transition metal dichalcogenides. The films are grown under Te-rich conditions in an UHV MBE (DCA) vertical chamber. The base pressure of the system is  $\sim 5 \times 10^{-10} \text{ Torr}$ . Te (99.999%) is evaporated from Knudsen cell. Hf 99.9% (metal basis excluding Zr, Zr nominal 2%) and Zr 99.8% (metal basis excluding Hf, Hf nominal 4%) metals are co-evaporated from two different electron guns. ARPES measurements were carried out at room temperature with a 100 mm hemispherical electron analyzer equipped with a 2D CCD detector (SPECS) without breaking the vacuum. The He I (21.22 eV) resonant line is used to excite photoelectrons. The energy resolution of the system is better than 40 meV with a polar angle step of 1°.

After the cleaning process, a  $2 \times 2$  reconstruction of the  $\text{InAs}(111)$  surface is observed by RHEED [Fig. 6(a)], as expected for a clean (oxygen-free) In-terminated  $\text{InAs}(111)$ . The streaky patterns of 17 monolayers  $\text{Hf}_{0.2}\text{Zr}_{0.8}\text{Te}_2$  films along the  $[1\bar{1}0]$  and  $[112]$   $\text{InAs}$  azimuths indicate smooth, well ordered surfaces with no rotational domains, aligned in-plane with the  $\text{InAs}(111)$  substrate, which is characteristic of vdW epitaxial growth. The surface morphology of the 17 monolayers  $\text{Hf}_{0.2}\text{Zr}_{0.8}\text{Te}_2$  film on  $\text{InAs}(111)$  is examined by *in situ* room-temperature ultra-high vacuum scanning tunneling microscopy (UHV-STM). The scanning conditions are  $V = 200 \text{ mV}$  and  $I = 400 \text{ pA}$ . Figure 6(b) shows a  $500 \times 500 \text{ nm}^2$  area scan of the sample. It can be inferred that  $\text{Hf}_{0.2}\text{Zr}_{0.8}\text{Te}_2$  is grown in the form of two-dimensional islands with an average surface roughness of  $\sim 3.5 \text{ \AA}$ , which is consistent with the  $\text{InAs}$  atomic step previously observed in epitaxial  $\text{ZrTe}_2$ <sup>18</sup> and  $\text{MoTe}_2$ .<sup>54</sup>

The band structure of 17 layers  $\text{Hf}_{0.2}\text{Zr}_{0.8}\text{Te}_2$  is imaged along the  $\Gamma$ M direction of the BZ (Fig. 7). The valence band exhibits a Dirac-like cone dispersion with the cone tip touching the Fermi

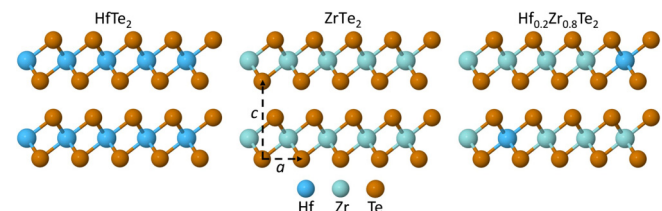
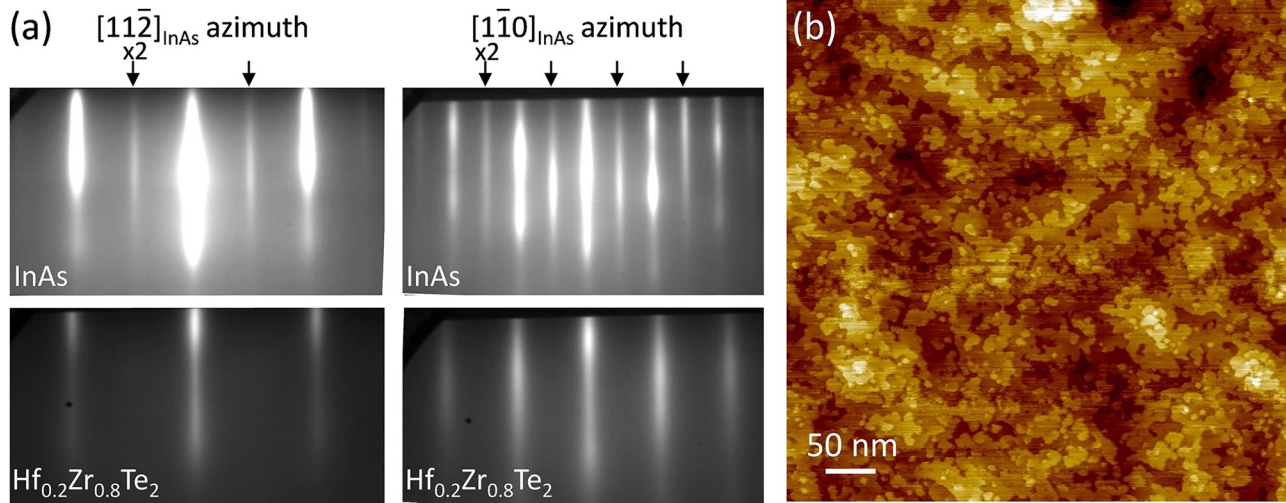


FIG. 5. Schematic illustration of  $\text{HfTe}_2$ ,  $\text{ZrTe}_2$ , and  $\text{Hf}_{0.2}\text{Zr}_{0.8}\text{Te}_2$  crystal structures. The Hf atoms are randomly placed inside the  $\text{Hf}_{0.2}\text{Zr}_{0.8}\text{Te}_2$  crystal.



**FIG. 6.** (a) RHEED patterns of the InAs(111) substrate and 17 monolayers  $\text{Hf}_{0.2}\text{Zr}_{0.8}\text{Te}_2$  films along the InAs $[\bar{1}10]$  and  $[\bar{1}1\bar{2}]$  azimuths. (b)  $500 \times 500 \text{ nm}^2$  STM image of 17 monolayers  $\text{Hf}_{0.2}\text{Zr}_{0.8}\text{Te}_2$  on InAs(111).

level which is similar to what has been observed in epitaxial  $\text{HfTe}_2$ <sup>17</sup> and  $\text{ZrTe}_2$ .<sup>18</sup> On the other hand, these observations are notably different than the theoretical predictions that the DP is located around 0.63 eV above the  $E_F$ . This is also in contrast to what is observed in the band structure of  $\text{HfTe}_2$  and  $\text{ZrTe}_2$  bulk single crystals imaged by synchrotron ARPES.<sup>19–22</sup> This difference

may be attributed to a substrate induced effect in the epitaxial few-layer film. A possible doping of the epitaxial films originating from the InAs(111) substrate could shift the Fermi level upward, allowing the observation of the linear band dispersions up to the tip of the Dirac cone. The cone-like band overlaps with a parabolic one located at the M point, indicating semimetallic character. The  $k_x$ – $k_y$  constant energy contours are also measured, where parts of the Fermi surface at different binding energies below the Fermi level are imaged. The conical shaped band around the zone center ( $\Gamma$  point) is visible and indicated with white dashed lines which intersect at the Dirac point at the Fermi level. Using  $E = \hbar v_F k$ , the Fermi velocity  $v_F$  can be estimated to be  $\sim 0.6 \times 10^6 \text{ m/s}$ , a value similar to that obtained in the case of  $\text{HfTe}_2$  and  $\text{ZrTe}_2$  epitaxial films.<sup>17,18</sup>

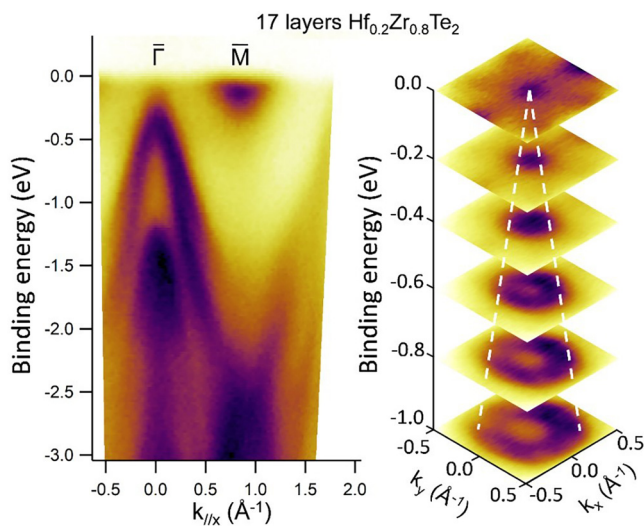


**FIG. 7.** ARPES spectra and  $k_x$ – $k_y$  energy contour plots at different binding energies of 17 layers  $\text{Hf}_{0.2}\text{Zr}_{0.8}\text{Te}_2$  along the  $\Gamma\text{M}$  direction of the BZ using the He I resonance line at 22.21 eV. The white dashed lines are guides to the eye that indicate the cone-like dispersion of the valence bands which intersect at the Dirac point.

#### IV. CONCLUSIONS

In this work, *ab initio* calculations indicate that  $\text{HfTe}_2$  is a type-I DSM with a point-like Fermi surface, while  $\text{ZrTe}_2$  is a type-II DSM with needle-like electron and hole pockets touching at the DP. A new alloy  $\text{Hf}_x\text{Zr}_{1-x}\text{Te}_2$  is predicted with a type-III Dirac cone emerging at  $x = 0.2$  with a line-like Fermi surface. An in-plane compressive strain is also applied in order to obtain the type-III phase. This strain could be used to switch between the two types of DSM. Epitaxial  $\text{Hf}_{0.2}\text{Zr}_{0.8}\text{Te}_2$  films are successfully grown on InAs(111) substrates by MBE. ARPES measurements indicate that  $\text{Hf}_{0.2}\text{Zr}_{0.8}\text{Te}_2$  films have semimetallic character with the valence bands exhibiting a linear dispersion in  $k$ -space, thus indicating topological Dirac semimetal behavior. The top of Dirac cone touches the Fermi level, which is notably different than theory which predicts the DP at an energy well above the Fermi level. Although, further studies are needed with synchrotron ARPES in order to visualize the  $k_z$  dispersion of the energy bands by varying the photon energy, these observations provide evidence that the

type-III topological DP, predicted by theoretical calculations, naturally lies at—or very close to—the Fermi level.

## ACKNOWLEDGMENTS

This work was supported by the Horizon 2020 projects SKYTOP “Skyrmion—Topological Insulator and Weyl Semimetal Technology” (FETPROACT-2018-01, No. 824123) and MSCA ITN SMART\_X 860553, the FLAG-ERA project MELoDICA, the Hellenic Foundation for Research and Innovation and the General Secretariat for Research and Technology, under Grant No. 435 (2D-TOP). We also acknowledge the computational time granted from the Greek Research and Technology Network in the National High-Performance Computing facility ARIS under project “2D-TOP” and we thank Professor Phivos Mavropoulos for discussions.

## DATA AVAILABILITY

The data that support the findings of this study are available from the corresponding authors upon reasonable request.

## REFERENCES

- <sup>1</sup>N. P. Armitage, E. J. Mele, and A. Vishwanath, *Rev. Mod. Phys.* **90**, 015001 (2018), and references therein.
- <sup>2</sup>G. E. Volovik, *JETP Lett.* **104**, 645 (2016).
- <sup>3</sup>G. E. Volovik and K. Zhang, *J. Low Temp. Phys.* **189**, 276 (2017).
- <sup>4</sup>T. Mizoguchi and Y. Hatsugai, *J. Phys. Soc. Jpn.* **89**, 103704 (2020).
- <sup>5</sup>I. M. Lifshitz, *Sov. Phys. JETP* **11**, 1130 (1960).
- <sup>6</sup>G. E. Volovik, *Phys. Usp.* **61**, 89 (2018).
- <sup>7</sup>Y. Zhang, C. Wang, L. Yu, G. Liu, A. Liang, J. Huang, S. Nie, X. Sun, Y. Zhang, B. Shen, J. Liu, H. Weng, L. Zhao, G. Chen, X. Jia, C. Hu, Y. Ding, W. Zhao, Q. Gao, C. Li, S. He, L. Zhao, F. Zhang, S. Zhang, F. Yang, Z. Wang, Q. Peng, X. Dai, Z. Fang, Z. Xu, C. Chen, and X. J. Zhou, *Nat. Commun.* **8**, 15512 (2017).
- <sup>8</sup>H. Chi, C. Zhang, G. Gu, D. E. Kharzeev, X. Dai, and Q. Li, *New J. Phys.* **9**, 015005 (2017).
- <sup>9</sup>Y. Zhang, C. Wang, G. Liu, A. Liang, L. Zhao, J. Huang, Q. Gao, B. Shen, J. Liu, C. Hu, W. Zhao, G. Chen, X. Jia, L. Yu, L. Zhao, S. He, F. Zhang, S. Zhang, F. Yang, Z. Wang, Q. Peng, Z. Xu, C. Chen, and X. Zhou, *Sci. Bull.* **62**, 950 (2017).
- <sup>10</sup>F. Caglieris, C. Wuttke, S. Sykora, V. Süß, C. Shekhar, C. Felser, B. Büchner, and C. Hess, *Phys. Rev. B* **98**, 201107(R) (2018).
- <sup>11</sup>H. Liu, J.-T. Sun, C. Song, H. Huang, F. Liu, and S. Meng, *Chin. Phys. Lett.* **27**, 067101 (2020).
- <sup>12</sup>H. Huang, K.-H. Jin, and F. Liu, *Phys. Rev. B* **98**, 121110 (2018).
- <sup>13</sup>S. Fragkos, R. Sant, C. Alvarez, E. Golias, J. Marquez-Velasco, P. Tsipas, D. Tsoutsou, S. Aminalragia-Giamini, E. Xenogiannopoulou, H. Okuno, G. Renaud, O. Rader, and A. Dimoulas, *Phys. Rev. Mater.* **3**, 104201 (2019).
- <sup>14</sup>M. Miličević, G. Montambaux, T. Ozawa, O. Jamadi, B. Real, I. Sagnes, A. Lemaître, L. Le Gratiet, A. Harouri, J. Bloch, and A. Amo, *Phys. Rev. X* **9**, 031010 (2019).
- <sup>15</sup>Z. K. Liu, B. Zhou, Y. Zhang, Z. J. Wang, H. M. Weng, D. Prabhakaran, S.-K. Mo, Z. X. Shen, Z. Fang, X. Dai, Z. Hussain, and Y. L. Chen, *Science* **343**, 864 (2014).
- <sup>16</sup>Z. K. Liu, J. Jiang, B. Zhou, Z. J. Wang, Y. Zhang, H. M. Weng, D. Prabhakaran, S.-K. Mo, H. Peng, P. Dudin, T. Kim, M. Hoesch, Z. Fang, X. Dai, Z. X. Shen, D. L. Feng, Z. Hussain, and Y. L. Chen, *Nat. Mater.* **13**, 677 (2014).
- <sup>17</sup>S. Aminalragia-Giamini, J. Marquez-Velasco, P. Tsipas, D. Tsoutsou, G. Renaud, and A. Dimoulas, *2D Mater.* **4**, 015001 (2017).
- <sup>18</sup>P. Tsipas, D. Tsoutsou, S. Fragkos, R. Sant, C. Alvarez, H. Okuno, G. Renaud, R. Alcotte, T. Baron, and A. Dimoulas, *ACS Nano* **12**, 1696 (2018).
- <sup>19</sup>Y. Nakata, K. Sugawara, A. Chainani, K. Yamauchi, K. Nakayama, S. Souma, P.-Y. Chuang, C.-M. Cheng, T. Oguchi, K. Ueno, T. Takahashi, and T. Sato, *Phys. Rev. Mater.* **3**, 071001 (2019).
- <sup>20</sup>Z. E. El Youbi, S. W. Jung, S. Mukherjee, M. Fanciulli, J. Schusser, O. Heckmann, C. Richter, J. Minár, K. Hricovini, M. D. Watson, and C. Cacho, *Phys. Rev. B* **101**, 235431 (2020).
- <sup>21</sup>B. Zhang, Z. Muhammad, P. Wang, S. Cui, Y. Li, S. Wang, Y. Wu, Z. Liu, H. Zhu, Y. Liu, G. Zhang, D. Liu, L. Song, and Z. Sun, *J. Phys. Chem. C* **124**, 16561 (2020).
- <sup>22</sup>I. Kar, J. Chatterjee, L. Harnagea, Y. Kushnirenko, A. V. Fedorov, D. Shrivastava, B. Büchner, P. Mahadevan, and S. Thirupathiah, *Phys. Rev. B* **101**, 165122 (2020).
- <sup>23</sup>S. Mangelsen, P. G. Naumov, O. I. Barkalov, S. A. Medvedev, W. Schnelle, M. Bobnar, S. Mankovsky, S. Polesya, C. Näther, H. Ebert, and W. Bensch, *Phys. Rev. B* **96**, 205148 (2017).
- <sup>24</sup>S. M. Ng, H. Wang, Y. Liu, H. F. Wong, H. M. Yau, C. H. Suen, Z. H. Wu, C. W. Leung, and J.-Y. Dai, *ACS Nano* **14**, 7077 (2020).
- <sup>25</sup>H. Wang, C. H. Chan, C. H. Suen, S. P. Lau, and J.-Y. Dai, *ACS Nano* **13**, 6008 (2019).
- <sup>26</sup>M. G. Vergniory, L. Elcoro, C. Felser, N. Regnault, B. A. Bernevig, and Z. Wang, *Nature* **566**, 480 (2019).
- <sup>27</sup>B. Bradlyn, L. Elcoro, J. Cano, M. G. Vergniory, Z. Wang, C. Felser, M. I. Aroyo, and B. A. Bernevig, *Nature* **547**, 298 (2017).
- <sup>28</sup>T. Zhang, Y. Jiang, Z. Song, H. Huang, Y. He, Z. Fang, H. Weng, and C. Fang, *Nature* **566**, 475 (2019).
- <sup>29</sup>F. Tang, H. C. Po, A. Vishwanath, and X. Wan, *Nature* **566**, 486 (2019).
- <sup>30</sup>N. H. D. Khang, Y. Ueda, and P. N. Hai, *Nat. Mater.* **17**, 808 (2018).
- <sup>31</sup>Y. Wang, R. Ramaswamy, and H. Yang, *J. Phys. D: Appl. Phys.* **51**, 273002 (2018).
- <sup>32</sup>S. Shi, S. Liang, Z. Zhu, K. Cai, S. D. Pollard, Y. Wang, J. Wang, Q. Wang, P. He, J. Yu, G. Eda, G. Liang, and H. Yang, *Nat. Nanotechnol.* **14**, 945 (2019).
- <sup>33</sup>D. Chakraborty and P. Johari, *ACS Appl. Nano Mater.* **3**, 5160 (2020).
- <sup>34</sup>G. Kresse and J. Furthmüller, *Comput. Mater. Sci.* **6**, 15 (1996).
- <sup>35</sup>G. Kresse and J. Furthmüller, *Phys. Rev. B* **54**, 11169 (1996).
- <sup>36</sup>J. P. Perdew, K. Burke, and M. Ernzerhof, *Phys. Rev. Lett.* **77**, 3865 (1996).
- <sup>37</sup>H. J. Monkhorst and J. D. Pack, *Phys. Rev. B* **13**, 5188 (1976).
- <sup>38</sup>A. A. Mostofi, J. R. Yates, G. Pizzi, Y.-S. Lee, I. Souza, D. Vanderbilt, and N. Marzari, *Comput. Phys. Commun.* **185**, 2309 (2014).
- <sup>39</sup>G. Pizzi, V. Vitale, R. Arita, S. Blügel, F. Freimuth, G. Géranton, M. Gibertini, D. Gresch, C. Johnson, T. Koretsune, J. Ibañez-Azpiroz, H. Lee, J.-M. Lihm, D. Marchand, A. Marrazzo, Y. Mokrousov, J. I. Mustafa, Y. Nohara, Y. Nomura, L. Paulatto, S. Poncé, T. Ponweiser, J. Qiao, F. Thöle, S. S. Tsirkin, M. Wierzbowska, N. Marzari, D. Vanderbilt, I. Souza, A. A. Mostofi, and J. R. Yates, *J. Phys. Condens. Matter* **32**, 165902 (2020).
- <sup>40</sup>Q. S. Wu, S. N. Zhang, H.-F. Song, M. Troyer, and A. A. Soluyanov, *Comput. Phys. Commun.* **224**, 405 (2018).
- <sup>41</sup>M. G. Vergniory, L. Elcoro, Z. Wang, J. Cano, C. Felser, M. I. Aroyo, B. A. Bernevig, and B. Bradlyn, *Phys. Rev. E* **96**, 023310 (2017).
- <sup>42</sup>L. Elcoro, B. Bradlyn, Z. Wang, M. G. Vergniory, J. Cano, C. Felser, B. A. Bernevig, D. Orobengoa, G. de la Flor, and M. I. Aroyo, *J. Appl. Crystallogr.* **50**, 1457 (2017).
- <sup>43</sup>B.-J. Yang and N. Nagaosa, *Nat. Commun.* **5**, 4898 (2014).
- <sup>44</sup>S.-Y. Xu, Y. Xia, L. A. Wray, S. Jia, F. Meier, J. H. Dil, J. Osterwalder, B. Slomski, A. Bansil, H. Lin, R. J. Cava, and M. Z. Hasan, *Science* **332**, 560 (2011).
- <sup>45</sup>T.-R. Chang, S.-Y. Xu, G. Chang, C.-C. Lee, S.-M. Huang, B.-K. Wang, G. Bian, H. Zheng, D. S. Sanchez, I. Belopolski, N. Alidoust, M. Neupane, A. Bansil, H.-T. Jeng, H. Lin, and M. Z. Hasan, *Nat. Commun.* **7**, 10639 (2016).
- <sup>46</sup>I. Belopolski, D. S. Sanchez, Y. Ishida, X. Pan, P. Yu, S.-Y. Xu, G. Chang, T.-R. Chang, H. Zheng, N. Alidoust, G. Bian, M. Neupane, S.-M. Huang,

- C.-C. Lee, Y. Song, H. Bu, G. Wang, S. Li, G. Eda, H.-T. Jeng, T. Kondo, H. Lin, Z. Liu, F. Song, S. Shin, and M. Z. Hasan, *Nat. Commun.* **7**, 13643 (2016).
- <sup>47</sup>S. Alvarez, *Dalton Trans.* **42**, 8617 (2013).
- <sup>48</sup>J. C. Slater, *J. Chem. Phys.* **41**, 3199 (1964).
- <sup>49</sup>N. Marzari, A. A. Mostofi, J. R. Yates, I. Souza, and D. Vanderbilt, *Rev. Mod. Phys.* **84**, 1419 (2012).
- <sup>50</sup>G. W. Winkler, A. A. Soluyanov, and M. Troyer, *Phys. Rev. B* **93**, 035453 (2016).
- <sup>51</sup>M. Nakagawa, R.-J. Slager, S. Higashikawa, and T. Oka, *Phys. Rev. B* **101**, 075108 (2020).
- <sup>52</sup>A. A. Soluyanov and D. Vanderbilt, *Phys. Rev. B* **83**, 035108 (2011).
- <sup>53</sup>A. Taguchi and K. Kanisawa, *Appl. Surf. Sci.* **252**, 5263 (2006).
- <sup>54</sup>P. Tsipas, S. Fragkos, D. Tsoutsou, C. Alvarez, R. Sant, G. Renaud, H. Okuno, and A. Dimoulas, *Adv. Funct. Mater.* **28**, 1802084 (2019).
- <sup>55</sup>S. Fragkos, R. Sant, C. Alvarez, A. Bosak, P. Tsipas, D. Tsoutsou, H. Okuno, G. Renaud, and A. Dimoulas, *Adv. Mater. Interfaces* **6**, 1801850 (2019).